

Influence of Obliquely Propagating Monsoon Gravity Waves on Southern Polar Summer Mesosphere after Stratospheric Sudden Warmings in Winter Stratosphere

David Alexandre¹, Brentha Thurairajah², Scott L England², and Chihoko Y. Cullens³

¹Virginia Tech

²Virginia Polytechnic Institute and State University

³University of California, Berkeley

November 23, 2022

Abstract

Oblique propagation of gravity waves (GWs) refers to latitudinal propagation (or vertical propagation away from their source) from the low latitude troposphere to the polar mesosphere. This propagation is not included in current gravity wave parameterization schemes, but may be an important component of the global dynamical structure. Previous studies have revealed a high correlation between observations of GW Momentum Flux (GWMF) from monsoon convection and Polar Mesospheric Clouds (PMCs) in the northern hemisphere. In this work, we report on data and model analysis of the effects of Stratospheric Sudden Warmings (SSWs) in the northern hemisphere, on the oblique propagation of GWs from the southern hemisphere tropics, that in turn influence PMCs in the southern summer mesosphere. In response to SSWs, vertical propagation of GWs from high-latitude winter hemisphere is at mid latitudes and appears more slanted toward the equator with increasing altitude, following the weaker stratospheric eastward jet. The oblique propagation of GWs from southern monsoon regions tends to start at higher altitudes with a sharper poleward slanted structure towards the summer mesosphere. The correlation between PMCs in summer southern hemisphere and the zonal GWMF from 50°N to 50°S exhibits a high-correlation pattern that connects the winter stratosphere with the summer mesosphere, indicating the influence of inter-hemispheric coupling mechanism. Temperature and wind anomalies suggest that the dynamics in winter hemisphere can influence the equatorial region, which in turn, can influence the oblique propagation of monsoon GWs.

1 **Influence of Obliquely Propagating Monsoon Gravity Waves on Southern Polar**
2 **Summer Mesosphere after Stratospheric Sudden Warmings in Winter Stratosphere**

3
4 **Enter authors here: D. Alexandre^{1,3}, B. Thuraiajah^{2,3}, S. L. England^{1,3}, and C. Y. Cullens⁴**

5 ¹Aerospace and Ocean Engineering department.

6 ²Electrical and Computer Engineering department.

7 ³Virginia Polytechnic Institute and State University, Blacksburg VA, USA.

8 ⁴University of California Berkeley, Berkeley CA, USA.

9
10 Corresponding author: David Alexandre (davida49@vt.edu)

11
12 **Key Points:**

- 13 • Polar mesospheric clouds in the SH correlate with gravity waves from monsoon regions
14 indicating oblique propagation of gravity waves in SH
- 15 • Gravity wave propagation in high-latitude winter hemisphere is at mid latitudes and slanted
16 equatorward during stratospheric sudden warmings
- 17 • Stratospheric sudden warmings appear to change the oblique propagation path of monsoon
18 generated gravity waves in summer hemisphere

19 Abstract

20 Oblique propagation of gravity waves (GWs) refers to latitudinal propagation (or vertical
21 propagation away from their source) from the low latitude troposphere to the polar mesosphere.
22 This propagation is not included in current gravity wave parameterization schemes, but may be
23 an important component of the global dynamical structure. Previous studies have revealed a high
24 correlation between observations of GW Momentum Flux (GWMF) from monsoon convection
25 and Polar Mesospheric Clouds (PMCs) in the northern hemisphere. In this work, we report on
26 data and model analysis of the effects of Stratospheric Sudden Warmings (SSWs) in the northern
27 hemisphere, on the oblique propagation of GWs from the southern hemisphere tropics, that in
28 turn influence PMCs in the southern summer mesosphere. In response to SSWs, vertical
29 propagation of GWs from high-latitude winter hemisphere is at mid latitudes and appears more
30 slanted toward the equator with increasing altitude, following the weaker stratospheric eastward
31 jet. The oblique propagation of GWs from southern monsoon regions tends to start at higher
32 altitudes with a sharper poleward slanted structure towards the summer mesosphere. The
33 correlation between PMCs in summer southern hemisphere and the zonal GWMF from 50°N to
34 50°S exhibits a high-correlation pattern that connects the winter stratosphere with the summer
35 mesosphere, indicating the influence of inter-hemispheric coupling mechanism. Temperature and
36 wind anomalies suggest that the dynamics in winter hemisphere can influence the equatorial
37 region, which in turn, can influence the oblique propagation of monsoon GWs.

38

39 Plain Language Summary

40 Propagation of waves throughout Earth atmosphere is a key phenomenon to understanding the
41 atmosphere dynamics, as it changes temperature, pressure, density and composition. Due to
42 exponentially decreasing density, amplitude and energy carried by these waves increase
43 exponentially as they propagate vertically. When waves break, their energy is released,
44 transferred to the background flow. Gravity Waves (GWs) with small horizontal wavelength can
45 propagate up to the middle atmosphere but are too small to be resolved by most global-scale
46 atmospheric models. The deep convection from monsoon regions is known as major source of
47 mesospheric GWs and previous studies on summer northern hemisphere have shown that
48 monsoon GWs tend to propagate obliquely from low-latitude stratopause up to high-latitude
49 mesopause. We focus this study on the summer southern hemisphere and the Inter-Hemispheric
50 Coupling (IHC) between the summer mesopause where Polar Mesospheric Clouds (PMCs) form,
51 and the winter stratosphere where sudden warmings occur and change the IHC pattern described
52 by previous studies. PMCs are excellent indicators of atmospheric changes and their correlations
53 with wind, temperature and GW momentum flux highlight the consequences of anomalies in
54 winter stratosphere, such as warmings, on the oblique propagation of GWs that influence the
55 PMC formation in summertime southern hemisphere.

56

57 **1 Introduction**

58 The dynamics significant to the coupling between atmospheric regions involve the
59 generation, propagation, and modulation of tides, Planetary Waves (PWs), and Gravity Waves
60 (GWs). Of note are dynamical processes associated with GWs, since these waves are the least
61 understood, due to the need to parameterize these waves in global climate models due to their
62 small scales. This study contributes to the understanding of the coupling between atmospheric
63 regions, specifically between the tropical stratosphere, a source of monsoon GWs, and high-
64 latitude mesosphere, where Polar Mesospheric Clouds (PMCs) form (Rapp et al., 2002). Sato et
65 al. (2009) first suggested that obliquely propagating GWs from monsoon regions can be an
66 important source of mesospheric GWs. More recently, Thurairajah et al. (2017 & 2020) used
67 satellite observations of PMCs and Gravity Wave Momentum Flux (GWMF) to study the effect
68 of obliquely propagating monsoon generated GWs on PMCs in the Northern Hemisphere (NH).
69 This work further investigates this topic focusing on the Southern Hemisphere (SH). PMCs
70 existence result from a dynamical refrigeration process of the summer mesopause region, driven
71 by GWs. In the winter hemisphere, Rossby waves from troposphere induce a poleward flow
72 called Brewer–Dobson circulation. The small-scale GWs, filtered out by this stratospheric
73 circulation, can propagate up to winter mesosphere and drive a poleward circulation that leads to
74 an equatorward circulation in summer mesosphere. This pole-to-pole circulation implies an
75 adiabatic expansion of the summer pole that cools the summer mesopause down enough to form
76 PMCs (Karlsson & Shepherd, 2018). While the propagation and the breaking processes of these
77 GWs are responsible for the cold summer mesopause, GWs have also been shown to cause the
78 sublimation of cloud particles leading to the destruction of PMC layers (e.g. Jensen & Thomas,
79 1994; Rapp et al., 2002; Gerrard et al., 2004; Chandran et al., 2012; Chu et al., 2009) and
80 enhancement of PMCs (Gao et al., 2018).

81 Sato et al. (2009) suggested that the largest source of mesospheric GWs in summer is the
82 deep convection from monsoon regions. From model simulations, Sato et al. (2009) showed that
83 the latitudinal shear in the prevailing westward jet, that has a slanted structure from the tropical
84 stratosphere to the polar mesosphere, could refract these monsoon generated GWs to the high-
85 altitude mesosphere. The oblique propagation (or latitudinal but vertical propagation away from
86 the source) has been reported in model studies (e.g. Kalisch et al., 2014) and observations (e.g.
87 Yasui et al., 2016; Thurairajah et al., 2017 & 2020). Yasui et al. (2016) used mesospheric wind
88 data from Antarctica and precipitation data from the tropics and found that a significant
89 component of the mesospheric GWs in high-latitude summer SH originates from tropical
90 convection (i.e. monsoon regions). Thurairajah et al. (2017 & 2020) used data from two satellite
91 instruments and showed a high correlation between observations of the GWMF from monsoon
92 GWs and PMCs in summer NH. This oblique propagation of GWs, from low-latitude
93 troposphere to high-latitude mesosphere, is not included in current gravity wave parameterization
94 schemes but may be an important component of the global dynamical structure of the
95 mesosphere.

96 Karlsson et al. (2007) found correlations between the temperature in the winter polar
97 stratosphere and the PMC Occurrence Frequency (PMC OF) observed in the opposite summer
98 hemisphere during Sudden Stratospheric Warmings (SSWs). SSWs are a consequence of
99 interactions between the atmospheric PWs and the mean flow in polar stratosphere (Matsuno,
100 1971). During SSWs, PWs induce a reversal of the polar stratospheric jet from eastward to
101 westward in winter hemisphere. The changes in the background wind alter the filtering of GWs

102 and, consequently, the directions of GWs drag from westward to eastward in the middle to high
103 latitudes ($\sim 60\text{-}90^\circ$) (e.g. Liu et al., 2002). The resulting equatorward circulation in the upper
104 mesosphere yields an upward flow in the mesosphere and a downward flow in the lower
105 thermosphere, respectively resulting in an adiabatic cooling and warming (Liu et al., 2002;
106 Cullens et al., 2015). In the Inter-Hemispheric Coupling (IHC) model presented by K rnich &
107 Becker (2010), amplification of PWs and associated changes in GWs in the winter polar region
108 alter the global residual circulation, changing the filtering of GWs in the summer hemisphere.

109 In this study, we analyze the influence of IHC mechanisms on PMCs by considering the
110 effects of SSWs, occurring in winter stratosphere, on the dynamics of the summer SH and on the
111 PMC activity in summer mesosphere. We investigate the combined influence of IHC and oblique
112 propagation of monsoon GWs on PMCs using data from November to March of 2010/2011 (a
113 no-SSW year) and 2012/2013 (a major SSW year). This paper is organized as follows. Section 2
114 presents the data and methods used in the derivation of GWMF, the process of locating the
115 monsoon regions in summer SH, the calculation of PMC OF, and the process of identifying
116 seasons with SSW events. Section 3 presents a comparison in PMC activity and GWMF activity
117 above monsoon regions from 2008 to 2014, in both the NH and the SH. Section 3 also describes
118 the monsoon regions in summer SH, the zonal mean zonal wind structure, the zonal mean
119 GWMF, the correlation between PMCs and GWMF, and the IHC analysis using wind and
120 temperature information. Section 4 contains a summary and conclusions.

121

122 **2 Data and Methodology**

123 **2.1 Monsoon Convection and Gravity Waves**

124 In this study, the location of the low-latitude source of GWs in summer SH is
125 investigated using two parameters: the rainfall rate (i.e. precipitation) and the Outgoing
126 Longwave Radiation (OLR). Both data have been shown to be a good proxy to estimate the
127 strength of the monsoon convection (Wright & Gille, 2011). The Tropical Rainfall Monitoring
128 Mission (TRMM) was designed to monitor and study tropical rainfall. It operated for 17 years,
129 including several mission extensions, before being decommissioned in April 15, 2015. The
130 rainfall rate data set is collected using the Dual-frequency Precipitation Radar (DPR) instrument.
131 The DPR instrument is an electronically scanning radar, operating at 13.8 GHz that measures the
132 3D rainfall distribution over both land and ocean, and define the layer depth of the precipitation.
133 The daily OLR information are collected by the National Oceanic and Atmospheric
134 Administration (NOAA) satellite using the Advanced Very High Resolution Radiometer
135 (AVHRR). NOAA-18 is a weather forecasting satellite run by NOAA and launched in 2005, into
136 a sun-synchronous orbit at an altitude of 854 km above the Earth. OLR data at the top of the
137 atmosphere are observed globally from the AVHRR instrument aboard NOAA-18. The daily raw
138 data are converted into a standardized anomaly index. Negative OLR are indicative of enhanced
139 convection and hence more cloud coverage. More convective activity implies higher, colder
140 cloud tops, which emit much less infrared radiation into space.

141 GW variability is derived from temperature observations from the Sounding of the
142 Atmosphere using Broadband Emission Radiometry (SABER) instrument onboard the
143 Thermosphere Ionosphere Mesosphere Energetics and Dynamics (TIMED) satellite (Russell et
144 al., 1999). Since 2002, the satellite TIMED is focused on the understanding of the energy

145 transfer into and out of the Mesosphere and Lower Thermosphere/Ionosphere (MLTI) region of
 146 the Earth's atmosphere (energetics), as well as the basic structure (i.e., pressure, temperature, and
 147 winds) that results from the energy transfer into the region (dynamics). SABER is a limb-
 148 scanning infrared radiometer that has provided global atmospheric measurements of temperature,
 149 pressure and geopotential height and trace species in the altitude range of 10-110 km. Due to the
 150 yaw cycle of TIMED, SABER can perform continuous measurements over the latitude range of
 151 50°N-50°S. Using the version 2.0 level 2A data product, we derive the GWMF from the zonal
 152 and meridional component of the GWMF and under the mid-frequency approximation (Ern et
 153 al., 2011) as:

$$GWMF = \frac{1}{2} \rho \frac{k_h}{m} \left(\frac{g}{N}\right)^2 \left(\frac{\hat{T}}{T_0}\right)^2$$

154 where ρ is the density of the background atmosphere, k_h is the horizontal wavenumber,
 155 m is the vertical wavenumber, g is the acceleration due to gravity, N is the Brunt Väisälä (i.e.
 156 buoyancy) frequency, \hat{T} is the temperature amplitude (after removing the PW wavenumber 1-5
 157 components), and T_0 is the background temperature. Note that the equation above only
 158 calculates the absolute values of GWMF (not its direction). This is because the satellite
 159 measurement track and the wave vector of the observed GW are not aligned, and therefore, the
 160 values of the horizontal wavelength will usually overestimate the true wavelength of the GW
 161 (Ern et al., 2011). Only the projection k of the horizontal wave vector can be determined, not the
 162 wave vector itself (Preusse et al., 2009). However, previous studies have shown that the above
 163 technique is reliable for GW related studies (e.g. Yamashita et al., 2013; Thuraiajah et al.,
 164 2017).

165 The background conditions including winds and temperature are obtained from Modern-
 166 Era Retrospective Analysis for Research and Applications (MERRA-2), a NASA atmospheric
 167 reanalysis for the satellite era using the Goddard Earth Observing System Model, Version 5
 168 (GEOS-5) with its Atmospheric Data Assimilation System (ADAS), version 5.12.4. The
 169 MERRA project focuses on historical climate analyses for a broad range of weather and climate
 170 time scales and places the NASA EOS suite of observations in a climate context. MERRA-2 data
 171 are available up to an altitude of ~77 km (~0.01 hPa). From this model, the zonal mean zonal
 172 wind speed and the zonal mean temperature have been computed to understand the IHC between
 173 the two regions.

174

175 2.2 Polar Mesospheric Clouds

176 PMC information is collected from the Cloud Imaging and Particle Size (CIPS)
 177 experiment on the Aeronomy of Ice in the Mesosphere (AIM) satellite (Russell et al., 1999). The
 178 version used is v05.10 level 3C (summary files) data product that provide season-long zonal
 179 averages of PMC occurrence. Since 2007, the primary goal of the AIM mission is to explore
 180 PMCs and to understand whether the clouds' ephemeral nature, and their variation over time, is
 181 related to Earth's changing climate. The mission collects data on cloud abundance, space
 182 distribution, and size of particles. CIPS is an ultraviolet imager that has provided PMC data
 183 (albedo, ice water content, occurrence frequency) in the latitude range of ~40-85° for both
 184 hemispheres (McClintock et al., 2008). To understand the seasonal variability in PMCs, we
 185 calculated the PMC OF by taking the sum of observed clouds over the total performed

186 observations. The PMC OF were daily averaged over the high-latitude region 65-85°N/S for the
 187 purpose of this study:

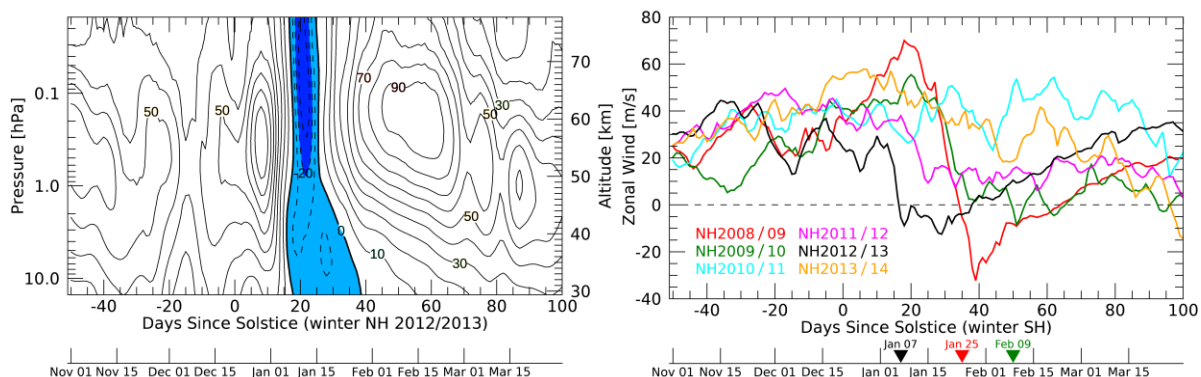
$$PMC\ OF = \frac{\sum \text{observed clouds}}{\sum \text{observations}} \%$$

188 For IHC study, Becker & Fritts (2006) and Karlsson et al. (2009) found a significant
 189 correlation between the vertical component of the Eliassen-Palm (EP) flux in the winter lower
 190 stratosphere and the temperature at the summer mesopause, but with a lag time that was altitude-
 191 dependent. Following the method used by Karlsson et al. (2009), we derived the lag times in
 192 PMC response to SSW using the PMC mean peak altitudes from Solar Occultation For Ice
 193 Experiment (SOFIE) instrument (Hervig et al., 2009) onboard AIM. AIM/SOFIE measures ice
 194 extinction profiles with a vertical resolution of ~1-2 km and the PMC peak ice extinction altitude
 195 at 3.064 μm gives us PMC altitudes along the PMC seasons.

196

197 2.3 Stratospheric Sudden Warmings

198 To identify SSWs, Charlton & Polvani (2007) used an algorithm that identifies SSWs
 199 based on the reversal of the zonal mean zonal wind from eastward to westward, at 60°N and at
 200 10 hPa. In addition to this wind condition, SSW years can be grouped by major-, minor- and no-
 201 SSW using the condition of a positive zonal mean temperature gradient between 60°N and 85°N
 202 at 10 hPa (e.g. Cullens et al., 2015). If both conditions are satisfied (westward wind and positive
 203 temperature gradient), a major SSW occurred. If one of the two conditions is satisfied, a minor
 204 SSW occurred. If none of the conditions is satisfied, no SSW occurred in the winter hemisphere
 205 for that particular year. Using the wind speed from MERRA-2, Figure 1 shows the zonal mean
 206 wind speed at 60°N from ~30 to ~80 km altitude during winter 2012/2013 (left) where a major
 207 SSW has been reported. The latter shows a clear reversal of the polar jet from eastward to
 208 westward (negative in blue) occurring between ~January 7th and ~January 28th 2013, Days Since
 209 Solstice (DSS) +17 and +38, respectively. Looking at the specific altitude of 10 hPa (~32 km),
 210 we can identify three years of SSW events from six winter seasons in NH from 2008/2009 to
 211 2013/2014, plotted on the right panel of Figure 1. To understand the effects of SSWs on the IHC
 212 pattern and on the propagation of GWs, we select summer SH 2010/2011 (cyan line) as the no-
 213 SSW season and summer SH 2012/2013 (black line) as the major-SSW season for the
 214 comparison made in this study.



215

216 **Figure 1.** Zonal mean wind speed at 60°N from ~30 to ~77 km altitude during winter 2012/2013
 217 (left) and at ~32 km (10 hPa) altitude during winter seasons from 2008/2009 to 2013/2014
 218 (right). The wind reversal is indicated by the blue area (negative = westward) in the left panel
 219 and by the triangular markers in the right panel.

220

221 3 Results

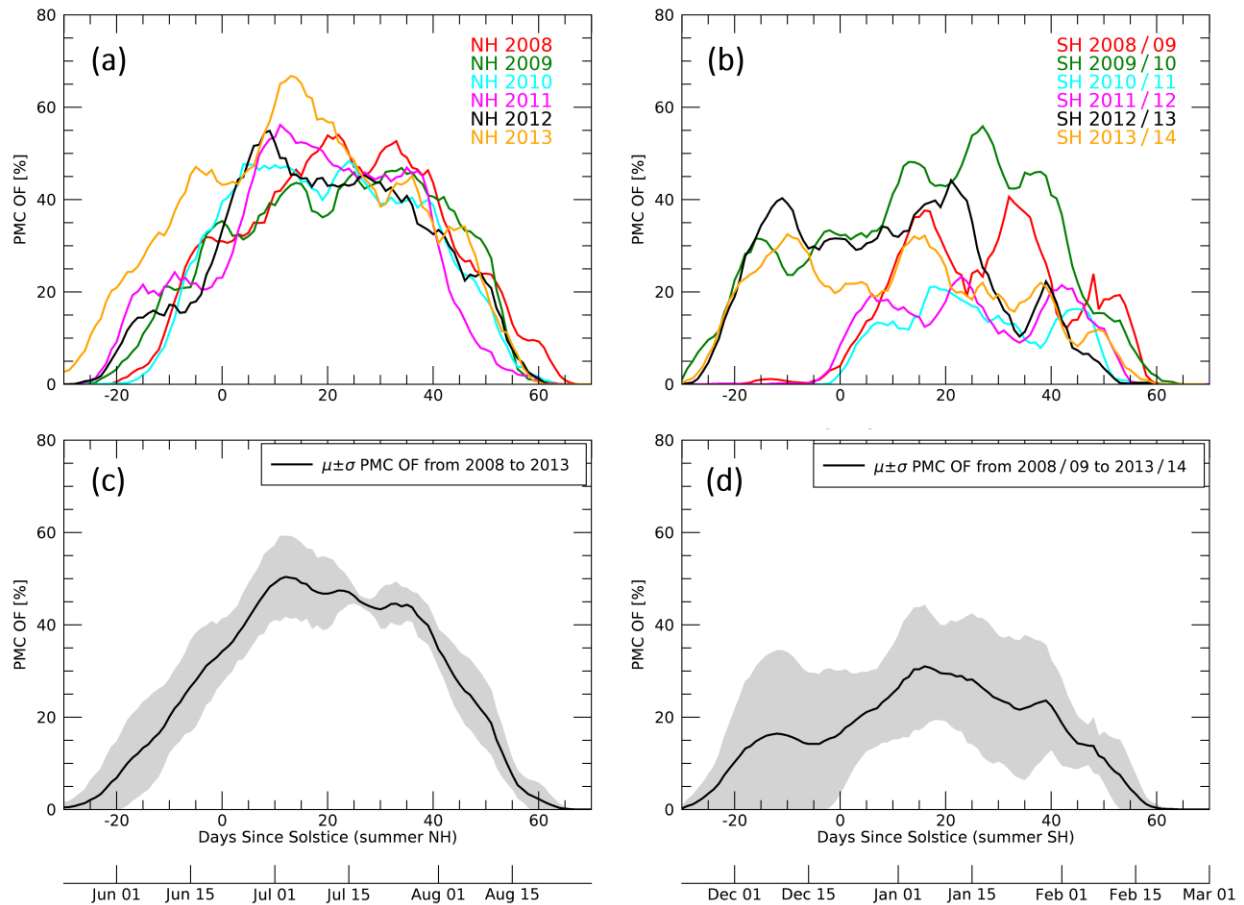
222 3.1 PMC Activity

223 To understand the variability in the occurrence of PMCs, we use AIM/CIPS observations
 224 from years 2008 to 2014, over the summer of both hemispheres. We compute the daily-averaged
 225 PMC OF over the latitude range of ~65-85°. Figure 2 shows the PMC OF over six PMC seasons
 226 in summer NH (Figure 2.a) and six PMC seasons in summer SH (Figure 2.b) from DSS -30 to
 227 +70. For these years, one can notice the uniformity in the seasonal distribution of PMCs in
 228 summer NH compared to SH. The seasons tend to start over a 10-day window between May 21st
 229 and June 1st and end between August 20th and August 28th. The average of these six seasons
 230 (Figure 2.c) follows a normal distribution with a daily standard deviation $\sigma \pm 7\%$ in the first half
 231 and $\sigma \pm 4\%$ in the second half of the season. This consistency seen in summer NH is not present
 232 in summer SH for the same range of years. Although the PMC seasons tend to end over a 10-day
 233 window between February 11th and February 21st, the start of the PMC season varies along years
 234 (Figure 2.b). PMC seasons start either around November 21st (2009, 2012 and 2013) or around
 235 mid-December (2008, 2010 and 2011). The resulting daily standard deviation (Figure 2.d)
 236 presents an asymmetric distribution along the PMC season, from November 21st (DSS -30) to
 237 February 29th/March 1st (DSS +70), with $\sigma \pm 12\%$ in the first half and $\sigma \pm 7\%$ in the second half of
 238 the season. The peak of PMC activity for both hemispheres tends to occur ~15 days after solstice
 239 (July 6th in NH, January 5th in SH) but the amplitude of PMC OF is significantly lower in
 240 summer SH than in summer NH (~20% less PMC OF).

241 Looking closely at the no-SSW and major-SSW years we use for our detailed study (i.e.
 242 summer SH 2010/2011 and 2012/2013, respectively), both PMC seasons end on February 12th
 243 (DSS +53). However, while the no-SSW season SH 2010/2011 (Figure 2.b, cyan line) starts on
 244 solstice, major-SSW season SH 2012/2013 (Figure 2.b, black line) starts 25 days earlier, on
 245 November 24th (DSS -27). The average PMC OF amplitude for the major-SSW season SH
 246 2012/2013 is also twice that of SH 2010/2011, but we observe a significant decrease from
 247 ~January 10th (DSS +20), when PMC OF is maximal, to ~January 20th (DSS +30), during
 248 2012/2013.

249 PMCs in NH tend to be larger and brighter, extending to lower latitudes and exhibiting
 250 less day-to-day and year-to-year variation than their SH counterparts (Karlsson & Shepherd,
 251 2018). Alexander & Rosenlof (1996) showed that the summer stratosphere is also warmer in the
 252 SH relative to the NH due to greater gravity wave induced forcing in the southern summer.
 253 Stratospheric hemispheric asymmetries have mesospheric counterparts whereby there would be
 254 weaker gravity wave drag in southern upper mesosphere, implying a warmer summer mesopause
 255 (Siskind et al., 2011). This has been suggested as a possible cause of the lower PMC OF in
 256 summer SH. Using the Solar Backscatter Ultraviolet (SBUV) satellite instruments, Benze et al.
 257 (2012) also found that, while the NH and SH PMC seasons on average start at the same time,
 258 variability in the SH onset date is twice as high as in the NH. Gumbel & Karlsson (2011) made

259 the same conclusion, using nine years of PMC observations by Odin satellite, where PMC
 260 seasons last from DSS -26 ± 3 to DSS 63 ± 3 in NH, and from DSS -24 ± 9 to DSS 58 ± 2 in SH.
 261 In addition to the confirmation of the role played by IHC from winter stratosphere on the
 262 seasonal, interannual and hemispheric variability of PMCs, Gumbel & Karlsson (2011) showed
 263 that the IHC from the summer stratosphere opens an upward pathway for polar vortex conditions
 264 to affect the summer mesosphere. Delayed start of PMC seasons can be explained by a persistent
 265 SH stratospheric jet, beyond DSS -30, and the late onset of PMC season in summer SH
 266 2010/2011 seen in Figure 2.b coincides with a long-lasting polar vortex conditions in the
 267 Antarctic stratosphere (Gumbel & Karlsson, 2011).



268

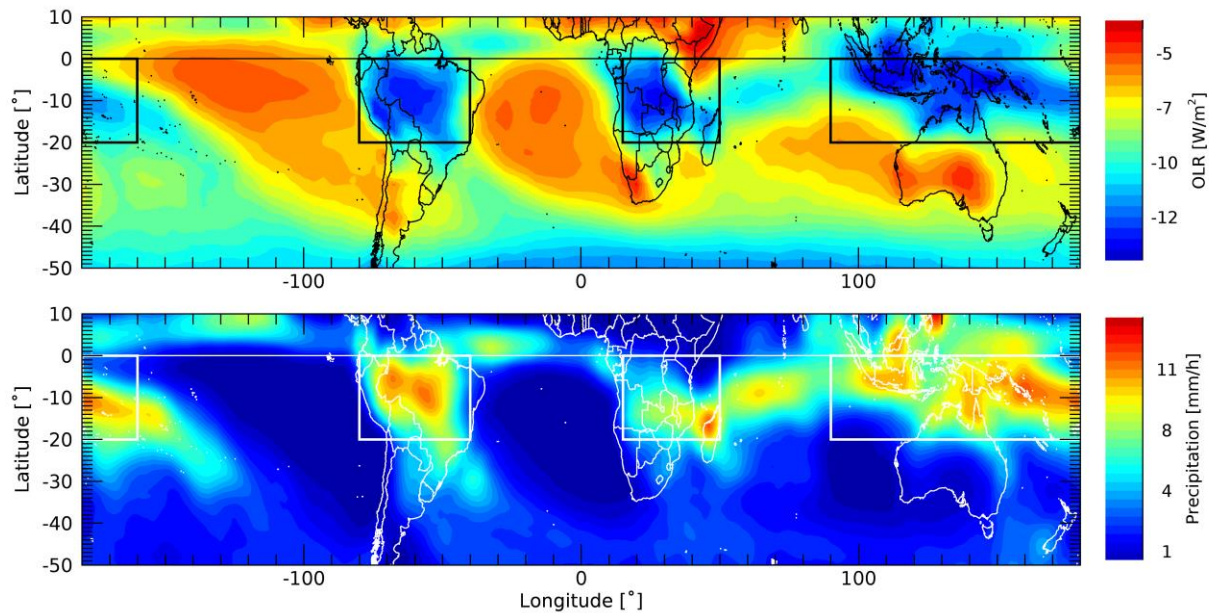
269 **Figure 2.** PMC activity in summer mesosphere using the daily-averaged PMC OF from
 270 AIM/CIPS over the $\sim 65\text{-}85^\circ\text{N/S}$ latitude band from 2008 to 2014 in summer NH (a) and summer
 271 SH (b). The mean and 1- σ standard deviation is shown in (c) and (d) for the NH and SH,
 272 respectively.

273

274 3.2 Monsoon Regions in SH

275 In order to locate monsoon regions in SH, we evaluate the strength of the monsoon
 276 convection by looking at the daily-averaged OLR from NOAA/AVHRR and the daily-averaged
 277 precipitation from TRMM/DPR. Figure 3 depicts both the OLR (top panel) and the precipitation

278 (bottom panel) for the month of January, averaged from 2008 to 2014. More convective activity
 279 implies higher, colder cloud tops, which emit much less infrared radiation into space. Therefore,
 280 a negative OLR is indicative of enhanced convection. From these two analyses, three highly
 281 convective regions have been identified in the SH: (1) Indonesia [$\sim 0\text{-}20^\circ\text{S}$, $\sim 90^\circ\text{-}160^\circ\text{E}$], (2)
 282 Central Africa [$\sim 0\text{-}20^\circ\text{S}$, $\sim 15\text{-}50^\circ\text{E}$] and (3) Amazonia [$\sim 0\text{-}20^\circ\text{S}$, $\sim 40\text{-}80^\circ\text{W}$]. The location of
 283 these regions in summer SH is consistent for individual years (not shown here) and agrees with
 284 the results obtained by Wright & Gille (2011), using the High Resolution Dynamics Limb
 285 Sounder (HIRDLS) onboard the NASA's Aura satellite (see Figure 2 and Table 1 in Wright &
 286 Gille, 2011). A parallel study on summer NH also showed the $\sim 0\text{-}20^\circ\text{N}$ latitude bin to be the
 287 most convective zonal area and a consistent monsoon region for the summer NH (not shown
 288 here).



289
 290 **Figure 3.** Daily-averaged OLR (top) from NOAA/AVHRR and daily-averaged precipitation
 291 (bottom) from TRMM/DPR in summer SH averaged over January from 2008 to 2014. Three
 292 monsoon regions: Indonesia, Central Africa and Amazonia are identified by boxes.

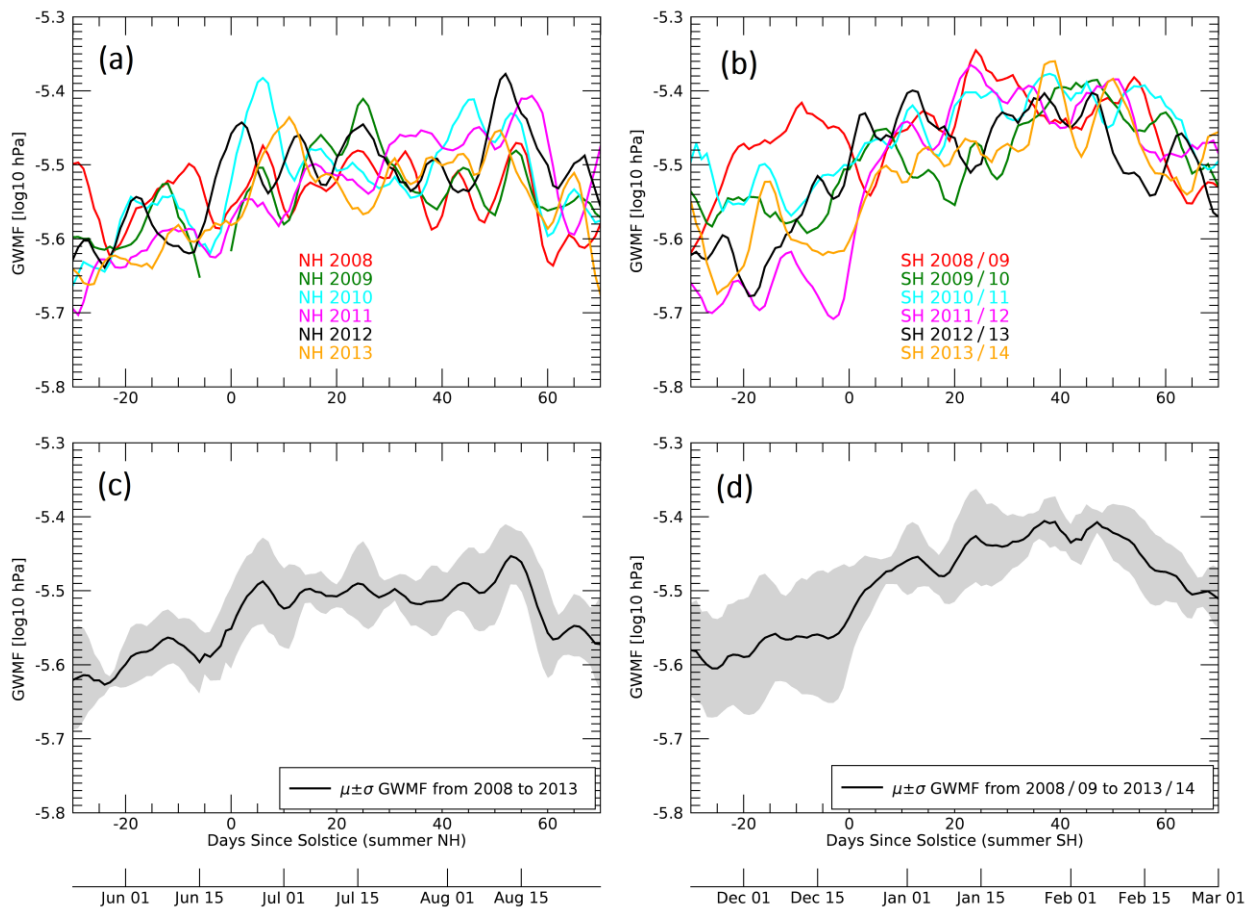
293

294 3.3 GWMF and Background Winds

295 TIMED/SABER performs continuous measurements over the latitude range of 50°N -
 296 50°S , which covers the monsoon regions. Due to the yaw cycle of TIMED, SABER observes the
 297 high-latitudes only for about half the PMC season. In the summer hemisphere, monsoon
 298 generated GWs have been shown to vertically propagate from their source in troposphere up to
 299 the stratopause (~ 50 km) where they focus into the mesospheric jet and can obliquely propagate
 300 to the high-latitude mesosphere (e.g. Sato et al., 2009; Thurairajah et al., 2017). Looking at 50
 301 km above the monsoon regions ($0\text{-}20^\circ\text{N/S}$) for both hemispheres, we explore the seasonal
 302 variability in the zonal mean GWMF from DSS -30 to DSS +70 in summer NH (Figure 4.a) and
 303 summer SH (Figure 4.b) for years 2008 to 2014. Figure 4.c and Figure 4.d show the
 304 corresponding average and 1-sigma standard deviation of the six seasons in summer NH and

305 summer SH, respectively. In both hemispheres, the momentum flux carried by GWs tends to
 306 increase until it reaches its maximum ~ 50 days after solstice. Note that, like the daily-averaged
 307 PMC OF (Figure 2.d), the daily standard deviation of GWMF above monsoon regions in SH
 308 (Figure 4.d) exhibits an asymmetric distribution with a distinct transition at solstice from large
 309 ($\sigma \sim 0.09 \log_{10} \text{ hPa}$ at DSS -5) to small ($\sigma \sim 0.02 \log_{10} \text{ hPa}$ at DSS +5) standard deviation. Despite
 310 this asymmetric pattern, both hemispheres present a relatively similar GWMF activity at the
 311 stratopause above their respective monsoon regions. Although monsoon regions in the widely
 312 studied summer NH present high momentum fluxes, the amplitude of GWMF above monsoon
 313 regions in summer SH is of equal if not higher than its NH counterpart for the same range of
 314 years and latitudes, consistent with results from Wright & Gille (2011).

315 Looking closely at the no-SSW and major-SSW years that we focus on in the next
 316 sections (i.e. SH 2010/2011 and SH 2012/2013, respectively), both years exhibit a similar
 317 GWMF seasonal distribution. The no-SSW season SH 2010/2011 (Figure 4.b, cyan line) presents
 318 a slightly higher GWMF ($+0.1 \log_{10} \text{ hPa}$) than the major-SSW season SH 2012/2013 (Figure 4.b,
 319 black line) between DSS -30 and -10 and between DSS +50 and +60.



321 **Figure 4.** GW seasonal variability in summer stratopause using the daily-averaged zonal mean
 322 GWMF from TIMED/SABER above the monsoon regions (latitude $\sim 0\text{-}20^\circ\text{N/S}$) and at ~ 50 km
 323 altitude from 2008 to 2014 in summer NH (a) and summer SH (b). The mean and $1\text{-}\sigma$ standard
 324 deviation is shown in (c) and (d) for the NH and SH, respectively.

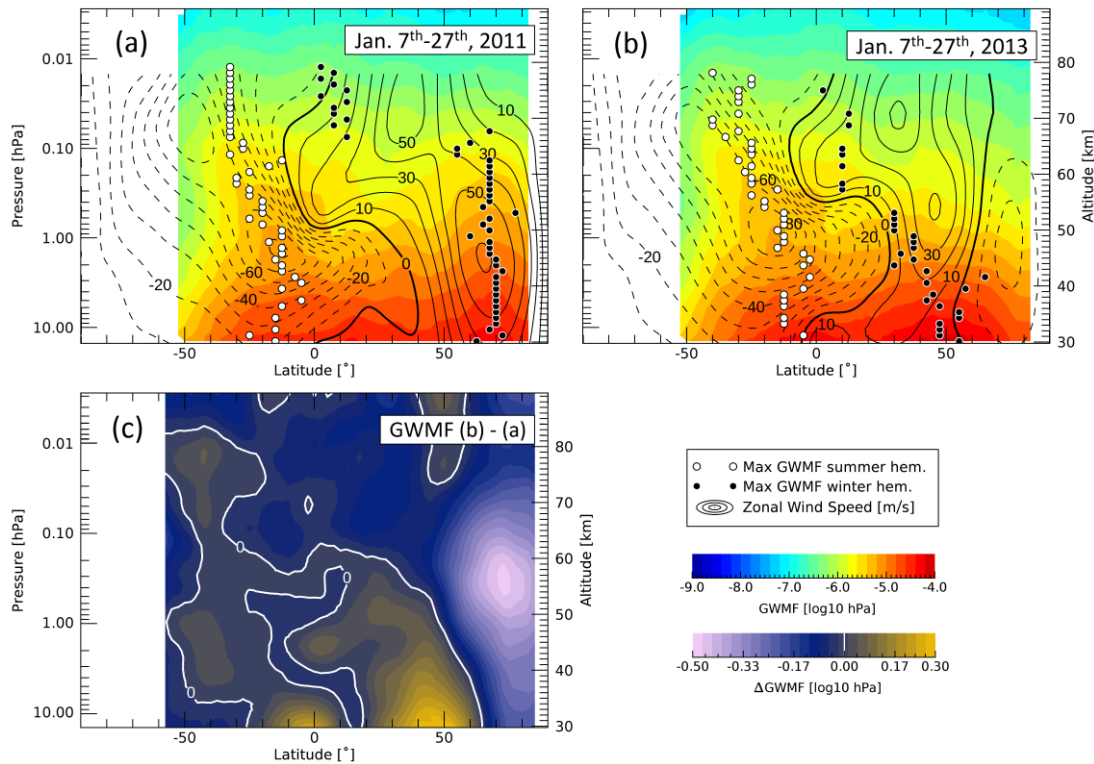
325

326 In order to investigate the effects of SSWs on the GWMF, we show the superposition of
 327 the zonal mean zonal wind speed from MERRA-2 on the zonal mean GWMF for the no-SSW
 328 year 2010/2011 and the major-SSW year 2012/2013, respectively in Figure 5.a and Figure 5.b.
 329 Both data are averaged for a 21-day period, starting on January 7th when SSW triggered in winter
 330 NH 2012/2013 (see Figure 1) and ending on January 27th, 20 days after the SSW. The altitude
 331 range for the zonal wind is limited to $\sim 30\text{-}77$ km by the model's limits and the latitude range for
 332 GWMF is limited to $\sim 50^\circ\text{S}\text{-}85^\circ\text{N}$ due to TIMED's yaw cycle during this 20-day period. The
 333 maximum GWMF, calculated at each 1-km altitude step, depicts the GW propagation in summer
 334 SH (white dots) and in winter NH (black dots). Figure 5.c shows the subtraction of the GWMF in
 335 no-SSW season 2010/2011 (Figure 5.a) from the GWMF in major-SSW season 2012/2013
 336 (Figure 5.b). In this difference plot, a positive [negative] value indicates an increase [decrease] in
 337 GWMF during the 20 days after SSW triggered in high-latitude winter NH.

338 In the winter hemisphere, the stratospheric eastward jet that prevails in high latitudes
 339 ($\sim 60\text{-}90^\circ$) can be attributed to the polar vortex, which is an important source of GWs (Ern et al.,
 340 2011). When no SSW is reported (e.g. winter NH 2010/2011, Figure 5.a), maximum GWMF in
 341 winter NH depicts the vertically propagating GWs in polar vortex at high latitudes ($\sim 70^\circ\text{N}$) and
 342 up to ~ 65 km altitude, following the strong eastward wind (> 50 m/s). When a major SSW
 343 occurs (e.g. winter NH 2012/2013, Figure 5.b), a reversal of the polar stratospheric jet is
 344 observed between latitudes $\sim 55\text{-}85^\circ\text{N}$ at 10 hPa altitude which reduces the strength of the
 345 eastward jet in winter tropical NH (< 30 m/s). The poleward flow (i.e. Brewer–Dobson
 346 circulation) at this altitude is strongly enhanced and, as a result of the so-induced warmer
 347 temperature and weaker eastward zonal wind, the westward GWs break at lower altitudes
 348 (Becker, 2012). The GWMF in the high-latitude winter stratosphere and winter mesosphere is
 349 therefore lower compared to the no-SSW winter NH (Figure 5.c). The reduction of $\sim 0.5 \log_{10}$
 350 hPa at approximately 55 km altitude and 75°N corresponds to a 68% decrease in GWMF (hPa).
 351 This reduced GW activity associated with SSW has been reported in previous studies (e.g.
 352 Siskind et al., 2010). The GWMF maximum at each altitude step no longer presents as a vertical
 353 pattern as seen for 2010/2011 (Figure 5.a) but is at mid latitudes ($\sim 50^\circ\text{N}$) and slanted toward the
 354 equator as altitude increases, following the weaker stratospheric eastward jet (Figure 5.b). Figure
 355 5.c also shows this increase in GWMF of almost 100% ($+0.3 \log_{10}$ hPa) from tropical winter
 356 stratosphere (~ 30 km altitude, $\sim 50^\circ\text{N}$ latitude) and along the same equatorward pattern described
 357 previously.

358 Above the monsoon regions (latitudes $\sim 0\text{-}20^\circ\text{S}$), GW propagation is quasi vertical up to
 359 the stratopause (~ 50 km). As the GWs propagate vertically, the GWMF decreases with altitude
 360 due to dissipation, they decelerate the jet and contribute to the slanted structure of the westward
 361 wind (Sato, et al., 2009). This westward wind associated with the monsoon circulation is slanted
 362 toward the high latitudes and allows the oblique propagation of the GWs generated from the low-
 363 latitude monsoon regions to the high-latitude mesosphere. The structure of the westward wind,
 364 slanted toward the summer pole and the mesospheric altitudes, is consistent for all years from
 365 2008 to 2014 (not shown here). In response to the SSW event and for the 20 days that follow, the

366 summer SH sees a significant increase in GWMF concentrated at ~ 30 km altitude above equator
 367 (Figure 5.c) of about 82% ($+0.26 \log_{10}$ hPa). Although the path depicted by the maximum
 368 GWMF (white dots) remains similar between summer SH 2010/2011 and summer SH 2012/2013
 369 (Figure 5.a and 5.b, respectively), we observe an increase of between 7% and 17% ($+0.03$ and
 370 $+0.07 \log_{10}$ hPa) in GWMF over a larger region, from ~ 30 km to ~ 80 km altitude and above the
 371 latitude bin ~ 30 - 50° S (Figure 5.c), but the path depicted by the maximum GWMF (white dots)
 372 remains similar between summer SH 2010/2011 and summer SH 2012/2013 (Figure 5.a and 5.b,
 373 respectively).



374

375 **Figure 5.** Zonal mean GWMF from TIMED/SABER (color) and zonal mean zonal wind speed
 376 from MERRA-2 (solid lines for eastward, dashed lines for westward) averaged from January 7th
 377 to January 27th in (a) 2011 and (b) 2013. GWMF maxima at each 1-km step altitude are depicted
 378 by white and black dots, respectively in summer SH and winter NH. (c) Difference in GWMF
 379 between no-SSW and major-SSW seasons by subtracting GWMF in (a) from GWMF in (b).

380

381 3.4 Correlation between PMCs and GWMF

382 Obliquely propagating GWs generated from low latitudes have been shown to have an
 383 influence on the polar summer mesosphere (Thurairajah et al., 2017 & 2020) and PMCs are
 384 sensitive indicators of such changes (Karlsson & Shepherd, 2018). While Thurairajah et al.,
 385 (2017 & 2020) presented results in the summer NH, here we study the instantaneous correlation
 386 between the time series of PMC OF in southern summer upper mesosphere (latitudes ~ 65 - 85° S)
 387 and GWMF measured over the latitude range 50° S- 50° N and the altitude range 30-90 km. Figure

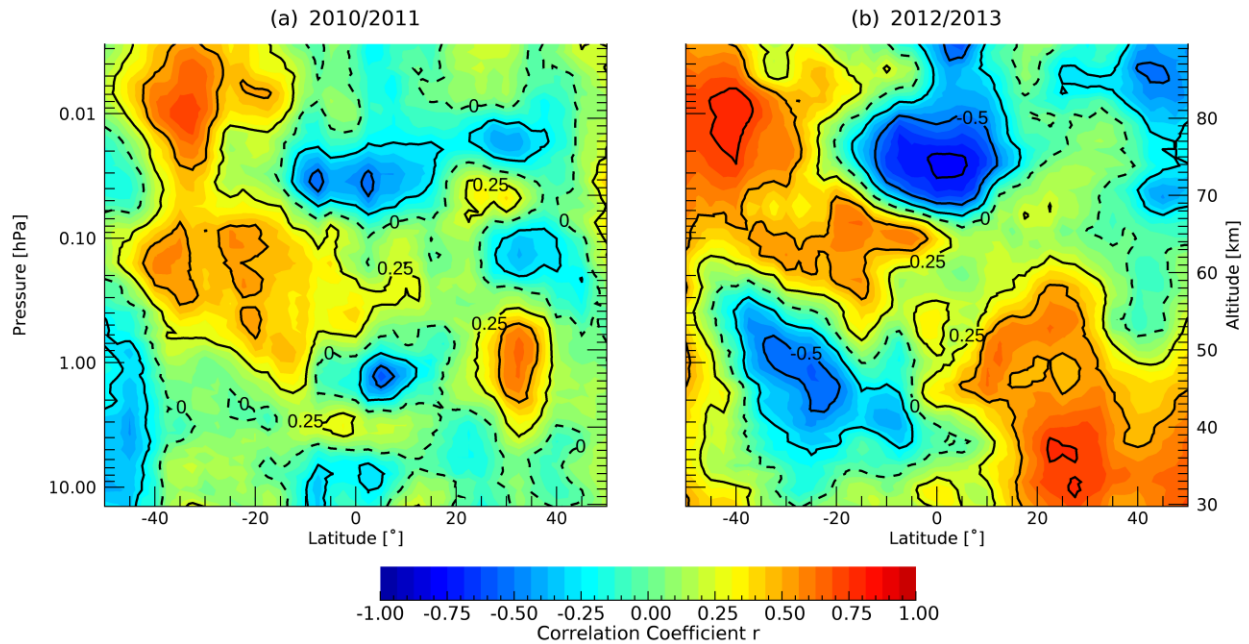
388 6.a and Figure 6.b depict the correlation coefficients, for 2010/2011 (no-SSW) and 2012/2013
389 (major-SSW), respectively, using data from November 21st (DSS -30) to March 1st (DSS +70).

390 In both seasons, the high-correlated region ($r > 0.5$) in mid-latitude summer mesosphere
391 is assumed (based on Figure 5) to be associated to the oblique propagation of GWs above
392 monsoon regions in low-latitude stratopause and slanted poleward to high-latitude mesopause.
393 We also observe a positive correlation in the winter hemisphere at lower altitudes that confirms
394 the link between the wintertime dynamics and the summer mesopause in the opposite
395 hemisphere. A positive correlation between PMC OF and GWMF means that an increase in GW
396 activity correlates with an increase in PMCs activity, and vice-versa.

397 When SSWs occur in winter stratosphere, the small region of high correlation ($r > 0.5$)
398 between PMCs and GWMF in winter stratopause (~ 50 km altitude, $\sim 32^\circ\text{N}$ latitude) seen in
399 Figure 6.a for the no-SSW year is replaced by a significantly larger area (~ 30 - 60 km altitude,
400 ~ 30 - 50°N latitude) of high correlation (Figure 6.b). It exhibits the same pattern seen in the
401 GWMF maxima (Figure 5.b, black dots) and GWMF difference between no-SSW and major-
402 SSW (Figure 5.c), starting at mid latitudes and slanted toward the equator as altitude increases.
403 This suggests that, although the GW activity in winter stratosphere is strongly reduced during
404 SSW events, with breaking occurring at lower altitudes, the PMC seasonal variations is more
405 correlated with the GWMF variations associated with the SSW dynamics. It demonstrates the
406 impact of winter GWs on the global mean meridional circulation and the summer mesopause
407 cooling (Karlsson & Becker, 2016).

408 The high-correlated region ($r > 0.5$) in mid-latitude summer mesosphere is replaced by a
409 larger area with higher coefficients when major SSW occur in summer SH 2012/2013 (Figure
410 6.b). If we evaluate the angle of this high correlation structure using a hypothetical straight line
411 slanted poleward, the resulting straight line stays in summer SH for the no-SSW season (Figure
412 6.a), connecting the low-latitude summer stratosphere (~ 30 km altitude, $\sim 10^\circ\text{S}$ latitude) with
413 mid-latitude mesopause (~ 80 km altitude, $\sim 30^\circ\text{S}$). However, the same method in Figure 6.b
414 exhibits a diagonal line that connects the mid-latitude winter stratosphere (~ 30 km altitude,
415 $\sim 50^\circ\text{N}$) with the mid-latitude summer mesosphere (~ 80 km altitude, $\sim 40^\circ\text{S}$ latitude). This
416 diagonal of positive correlations between PMCs and GWMF is between two large highly anti-
417 correlated regions ($r < 0.5$): the equatorial upper mesosphere (~ 75 km altitude, $\sim 0^\circ$ latitude) and
418 the low-latitude upper stratosphere (~ 50 km altitude, ~ 20 - 40°S latitude). These observations
419 suggest that, despite a similar zonal mean westward wind structure prevailing in summer SH for
420 a 20-day period between 2010/2011 and 2012/2013 (see Figure 5.a and 5.b), the major SSW,
421 occurring in winter stratosphere, changes GW activities in the SH. For the no-SSW season (e.g.
422 summer SH 2010/2011), the GWs from monsoon convection that are presumed to propagate
423 vertically and reach ~ 50 km altitude, then obliquely propagate following the poleward tilt of the
424 easterly jet that prevails in summer SH. This agrees with the results obtained in summer NH by
425 Thuraijajah et al. (2017). For the major-SSW season (e.g. summer SH 2012/2013), the oblique
426 propagation of monsoon GWs appears to be modified by the dynamics associated with the SSW
427 in the NH winter. The high correlation region, above monsoon regions, is at a higher altitude
428 above the stratopause (~ 65 km) and slanted poleward with a sharper angle in mesosphere.

429



430

431 **Figure 6.** Correlation coefficient between time series of PMC OF, observed by AIM/CIPS from
 432 southern summer mesopause (~ 84 km altitude, ~ 65 - 85° S latitude), and GWMF from
 433 TIMED/SABER over the meridional cross section (~ 30 - 90 km altitudes, $\sim 50^\circ$ S- 50° N latitudes),
 434 daily-averaged from DSS -30 to DSS +70 in (a) summer SH 2010/2011 and (b) summer SH
 435 2012/2013. Dashed lines denote the 0 and solid lines denote the ± 0.25 , ± 0.5 and ± 0.75
 436 correlation coefficients (r).

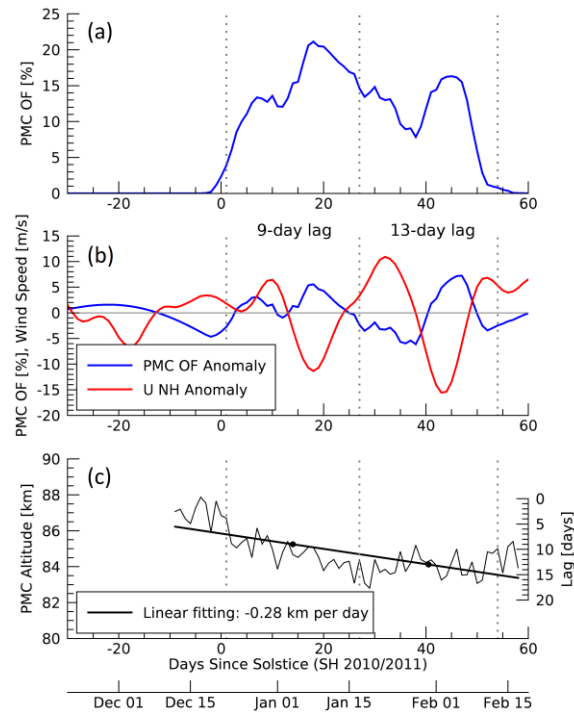
437

438 3.5 IHC analysis

439 Due to the yaw cycle of TIMED, no GWMF information is available in the high-latitude
 440 summer SH from January $\sim 15^{\text{th}}$ to March $\sim 15^{\text{th}}$, when SSWs usually occur in the opposite winter
 441 stratosphere (see Figure 5). Therefore, we investigate the effect of SSWs on the PMC region by
 442 comparing summer SH 2010/2011 (no-SSW) with summer SH 2012/2013 (major-SSW) within
 443 an IHC analysis, applying the method used by Karlsson et al. (2009) and graphically described
 444 by Figure 7. Here we use the zonal mean zonal wind (U) and the temperature (T) from MERRA-
 445 2, in the available altitude range (~ 0 - 77 km). Although the top altitude does not include the PMC
 446 altitudes, we can have a sense of change in U and T seen in IHC mechanism.

447 Following Karlsson et al. (2009), we first compare the PMC OF, averaged over latitudes
 448 65 - 85° S, with the zonal mean zonal wind, averaged over latitudes 59 - 61° N and altitudes 10 - 5
 449 hPa. At $\sim 60^\circ$ N, this altitude region is a good indicator of the variability in the winter stratosphere
 450 (Karlsson et al., 2009). Figure 7.a shows the PMC OF from AIM/CIPS for SH 2010/2011. Since
 451 the IHC of the middle atmosphere general circulation is characterized by a global anomaly
 452 pattern of the zonal mean temperature, this analysis uses the anomaly fields of PMCs, wind and
 453 temperature data ($\overline{PMC\ OF'}$, $\overline{U'}$ and $\overline{T'}$, respectively) which we derive by subtracting the 6^{th} -
 454 order polynomial fitting of the data from the data itself. Figure 7.b shows SH $\overline{PMC\ OF'}$ and NH
 455 $\overline{U'}$ for 2010/2011. By computing a time-lagged correlation between these two parameters, the
 456 highest correlation coefficient indicates two lag times. There is a 9-day lag in the first half of the

457 PMC season, and a 13-day lag in the second half of the PMC season. Halves of the PMC season
 458 are indicated by the dashed vertical lines in Figure 7. Karlsson et al. (2009) noted that the lag
 459 changes during the PMC season due to the associated change in PMC altitudes. Therefore, the
 460 resulting lag times are altitude-dependent. In Figure 7.c we show the PMC altitudes from
 461 AIM/SOFIE data. Using a linear fit of the PMC altitude variations, the two lag times are then
 462 used as two points on DSS +14 and +40 (i.e the median dates) to obtain an interpolated time
 463 varying lag along the PMC season.



464

465 **Figure 7.** (a) PMC OF from AIM/CIPS averaged over latitudes 65-85°S for SH 2010/2011, (b)
 466 anomaly fields of the PMC OF (blue) and the zonal mean zonal wind from MERRA-2, averaged
 467 over latitudes 59-61°N and altitudes 10-5 hPa (red), seen from November 21st to February 19th.
 468 (c) PMC altitudes from AIM/SOFIE. The linear fit is shown by the straight line.

469

470 From this method, we compare the correlation of PMC OF anomaly with the global zonal
 471 mean zonal wind and the zonal mean temperature anomaly fields from MERRA-2 for both
 472 summer SH 2010/2011 and summer SH 2012/2013 (see Figure 8 and 9, respectively). This
 473 correlation analysis is focused on data from November 21st (DSS -30) to March 1st (DSS +70).

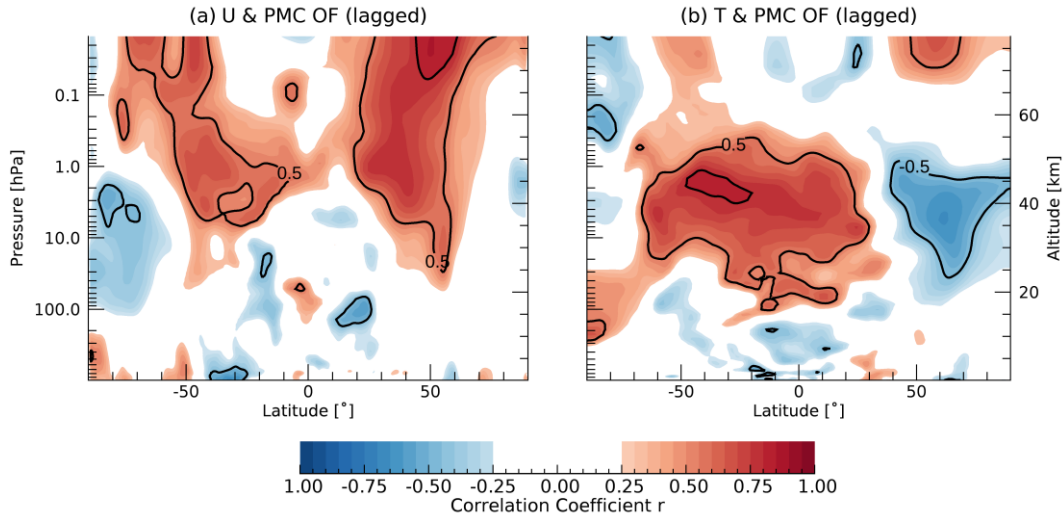
474 In Figures 8.a and 9.a, both the no-SSW and the major-SSW seasons show large areas of
 475 high correlation ($r > 0.5$) between $\overline{PMC\ OF'}$ and $\overline{U'}$. The area with strongest coefficients is
 476 located in the winter stratosphere, highly correlated with PMCs in summer mesopause and
 477 agreeing with IHC mechanism described by Karlsson et al. (2009). The second area of positive
 478 correlation between $\overline{PMC\ OF'}$ and $\overline{U'}$ is located in the opposite summer stratosphere and is due
 479 to dynamics in the winter stratosphere affecting the summer stratospheric flow. During SSW,
 480 these two positive correlation areas are enhanced (Figure 9.a) and the higher correlation with the
 481 eastward $\overline{U'}$, prevailing in high-latitude winter NH and weakened by SSW, suggests that PMC

482 day-to-day variations are significantly more correlated with anomalies caused by SSW that cross
 483 the equator via the meridional circulation.

484 In Figures 8.b and 9.b, both the no-SSW and the major-SSW seasons show a negative
 485 correlation between $\overline{PMC OF'}$ and $\overline{T'}$ in high-latitude winter stratosphere associated with a
 486 positive correlation in equatorial stratosphere and a positive correlation in polar winter
 487 mesosphere. This quadrupole structure agrees with previous IHC analyses. Karlsson et al. (2007)
 488 showed this positive/negative winter dipole pattern in the correlation between noctilucent cloud
 489 properties and stratospheric temperatures in winter stratosphere from July 2002 to January 2007.
 490 Due to higher PW activity in winter troposphere and stratosphere, high-latitude stratosphere and
 491 low-latitude mesosphere experience warming while high-latitude mesosphere and low-latitude
 492 stratosphere experience cooling. The deceleration of the zonal wind by PWs leads to a reduction
 493 of the net GW drag, responsible for driving the mesospheric meridional circulation (Becker &
 494 Fritts, 2006). The winter mesospheric meridional circulation being weaker, the high-latitude
 495 adiabatic heating is reduced and the high-latitude winter mesosphere is cooler during high PW
 496 activity. It also reduces the upwelling and increases temperature in equatorial mesosphere. In
 497 stratospheric altitudes, the Brewer-Dobson circulation warms the high latitudes up and cools the
 498 equatorial stratosphere down. In both seasons, the correlation between $\overline{PMC OF'}$ and $\overline{T'}$ tend to
 499 exhibit this quadrupole structure in winter hemisphere. However, the most important step for
 500 IHC consists of how anomalies, induced by SSWs, cross the equator. As the zonal wind does not
 501 change in summer stratosphere, the GW filtering remains the same between no-SSW and major-
 502 SSW season, and it allows large phase speed GWs to propagate up to mesosphere. In this region,
 503 the $\overline{U'}$ anomaly makes the background wind closer to the GW phase speed and induces wave
 504 breaking at lower altitudes, creating a downward shift of the GW drag associated with a
 505 downward shift of the upper branch of the residual circulation (Körnich & Becker, 2010). This
 506 leads to a positive $\overline{T'}$ anomaly in summer polar mesopause during SSWs.

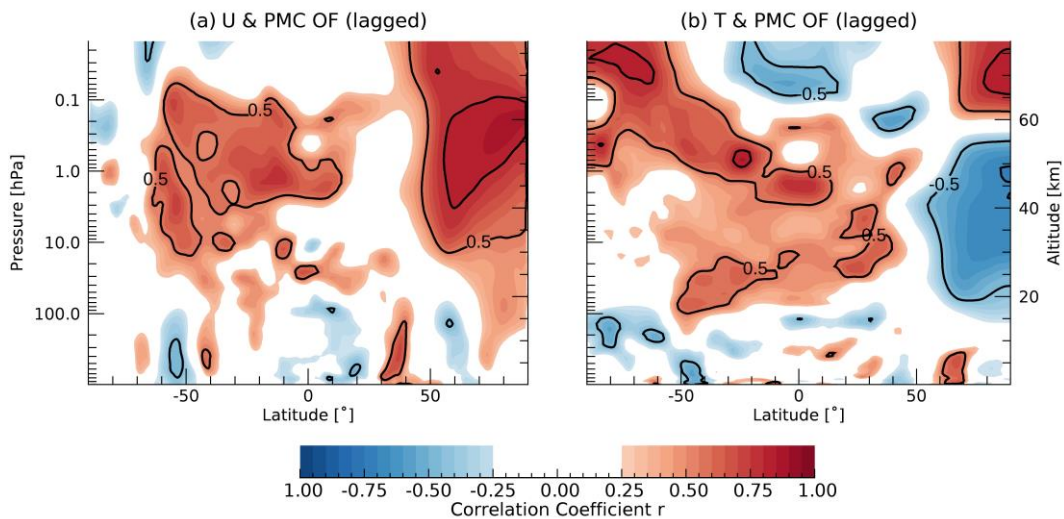
507 In addition to a strongly enhanced quadrupole structure in major-SSW season 2012/2013,
 508 we observe a strong positive correlation between $\overline{PMC OF'}$ and $\overline{T'}$ below the PMC region in
 509 Figure 9.b. This high-correlation area, concentrated only in the equatorial stratosphere for SH
 510 2010/2011 (Figure 8.b), extends towards high-latitude summer mesosphere for SH 2012/2013,
 511 depicting a pattern slanted poleward from low-latitude stratopause to high-latitude mesosphere
 512 (Figure 9.b). Knowing that a positive correlation with temperature can be associated to the
 513 destruction of PMC layers (Gumbel & Karlsson, 2011), this correlation using the adjusted-lag
 514 PMC OF explains the decrease in PMC OF occurring later in SH 2012/2013 season at DSS +20
 515 (see Figure 2.b). Siskind et al. (2011) have shown that a similar decrease in PMC activity at mid-
 516 season NH 2007 likely resulted from IHC due to enhanced PWs in the SH winter. Karlsson &
 517 Becker (2016) showed that winter GW activity reduces the net GW drag in the winter
 518 mesosphere, which then leads to a weaker winter residual circulation and a warmer summer
 519 polar mesosphere. The change in dynamics, induced by the major SSW and associated with the
 520 temperature patterns in Figure 8.b and 9.b, could also explain the change in the correlation
 521 pattern between PMC OF and GWMF in Figure 6.a and 6.b.

522
 523



524

525 **Figure 8.** Correlation coefficients of the lag-adjusted PMC OF anomaly with (a) the zonal mean
 526 zonal wind speed \bar{U}' and with (b) the zonal mean temperature \bar{T}' from MERRA-2, for summer
 527 SH 2010/2011 (no SSW). Black contours denote the ± 0.5 and ± 0.75 correlation coefficients (r).



528

529 **Figure 9.** Same as Figure 8 but for summer SH 2012/2013 (major SSW).

530

531 4 Summary and conclusions

532 Oblique propagation of GWs refers to the latitudinal propagation of GWs, from the
 533 summer stratosphere above the tropical monsoon convection source to the high-latitude summer
 534 mesosphere. Previous studies have been conducted in summer NH using a large range of PMC
 535 seasons and revealed a high correlation between observations of the GWMF from monsoon GWs
 536 and PMCs. Although this oblique propagation plays an important role in the global dynamical
 537 structure of the mesosphere, it is not included in GW parameterization schemes. Motivated by
 538 these studies, here we presented a combination of satellite observations and model to understand
 539 this atmospheric phenomenon in the summer SH. We compared six PMC seasons in summer NH
 540 and six PMC seasons in summer SH from 2008 to 2014. PMC OF in summer NH tends to

541 exhibit a normal distribution from DSS -30 to +70 but this consistency and symmetry was not
 542 present in the PMC OF in summer SH. PMCs in NH tend to be larger and brighter, extending to
 543 lower latitudes and exhibiting less day-to-day and year-to-year variation than their SH
 544 counterparts (Karlsson & Shepherd, 2018).

545 Knowing the largest source of GWs in summer troposphere to be the deep convection
 546 from monsoon regions (Sato et al., 2009), we measured the convection strength in summer SH.
 547 We identified three high-convective regions: (1) Indonesia [~ 0 - 20°S , $\sim 90^\circ\text{E}$ - 160°E], (2) Central
 548 Africa [~ 0 - 20°S , ~ 15 - 50°E] and (3) Amazonia [~ 0 - 20°S , ~ 40 - 80°W]. We then analyzed the
 549 daily-averaged zonal mean GWMF above these regions for both hemispheres from 2008 to 2014.
 550 Despite an asymmetric distribution in SH, which was also present in the daily-averaged PMC
 551 OF, GWMF amplitudes above monsoon regions in SH is as significant as its widely more studied
 552 NH counterparts are.

553 In addition to this hemispheric comparison, we were interested in the effects of the
 554 seasonal variability in the opposite winter NH. We identified years when SSWs (major and
 555 minor) occurred by looking at the polar jet reversal (from eastward to westward) at 60°N latitude
 556 and ~ 32 km (10 hPa) altitude using MERRA-2 winds. As a case of study, we focused the rest of
 557 our analysis on two PMC seasons in SH, 2010/2011 (no SSW was observed in the NH) and
 558 2012/2013 (major SSW occurred in the NH). We then compared the zonal mean GWMF and the
 559 zonal mean zonal wind speed between the two PMC seasons, averaged for 21 days starting on
 560 January 7th, when major SSW occurred in 2013. For no-SSW year (2010/2011), results
 561 confirmed the vertical propagation of GWs from polar vortex, focusing into the strong
 562 stratospheric eastward jet. In addition, oblique propagation of GWs from the southern monsoon
 563 regions to the southern mesosphere are shown, consistent with previous work on oblique
 564 propagation of GW in the NH. During the SSW in 2013, the eastward jet in winter NH is
 565 reversed to westward, and westward GWs tend to break at lower altitudes. The resulting lower
 566 GW activity in high-latitude stratosphere is shown by a 68% decrease in GWMF ($-0.5 \log_{10}$ hPa),
 567 at ~ 55 km and $\sim 75^\circ\text{N}$, compared to the no-SSW year. This decrease is counter-balanced by a
 568 significant increase in GWMF ($+0.3 \log_{10}$ hPa, $+100\%$ hPa) at ~ 30 km and $\sim 50^\circ\text{N}$. As a result,
 569 the maximum GWMF located at mid latitudes in stratosphere and slanted toward equator as
 570 altitude increases, following the weaker stratospheric eastward jet. Although the oblique
 571 propagation of GWs from southern monsoon regions, depicted by the maximum GWMF, is seen
 572 in both seasons (no-SSW and major-SSW), the GWMF at ~ 30 km above equator is shown to be
 573 82% greater ($+0.26 \log_{10}$ hPa) in major-SSW season than in no-SSW season. This increase in
 574 GWMF extended from ~ 30 km to ~ 80 km altitude and above the latitude bin ~ 30 - 50°S , between
 575 7% and 17% greater ($+0.03$ and $+0.07 \log_{10}$ hPa) in major-SSW season than in no-SSW season.

576 By investigating the correlation between daily-averaged PMC OF and zonal mean
 577 GWMF, three observations can be made regarding the effects of SSW. (1) Although the GWMF
 578 contribution in winter stratosphere is strongly reduced during SSWs, the PMC seasonal
 579 variations in the summer SH is highly correlated with these GWMF seasonal variations in NH.
 580 (2) This high-correlated region also exhibits the same pattern seen in the GWMF maxima (Figure
 581 5.b, black dots), located at mid latitudes and slanted toward the equator as altitude increases,
 582 following the weaker stratospheric eastward jet. (3) Despite a similar westward zonal wind
 583 structure in summer SH between both seasons, the major SSW changes the high-correlation
 584 structure of PMC OF – GWMF in summer mesosphere, which was associated to the propagation
 585 of monsoon generated GWs. The major-SSW summer SH 2012/2013 shows a pattern that starts

586 at higher altitude (~65 km) and is slanted poleward with a sharper angle in mesosphere,
 587 compared to the oblique propagation described by Thurairajah et al. (2017) and shown in the no-
 588 SSW summer SH 2010/2011.

589 Extending this study beyond the range of SABER at higher latitudes, we performed the
 590 IHC analysis following the method used by Karlsson et al. (2009), investigating the correlation
 591 of the day-to-day variability in PMC OF with the variability in the zonal mean zonal wind and
 592 temperature from MERRA-2. The comparison of both seasons showed agreements with the IHC
 593 mechanisms described in previous studies (Karlsson et al., 2007 ; 2009 ; 2016) and highlighted
 594 the influence of major SSWs in winter NH on PMCs in summer SH. The results obtained in
 595 summer SH 2012/2013 are similar to results obtained by Karlsson et al. (2009) in summer SH
 596 2007/2008, where major SSW has also been reported. (1) The strong correlation of adjusted-lag
 597 $\overline{PMC\ OF'}$ with high-latitude stratospheric wind $\overline{U'}$ is largely enhanced for major-SSW season ($|r|$
 598 +14%), suggesting that the day-to-day variability in PMCs is more correlated to SSW-induced
 599 anomalies that cross the equator via the meridional circulation. (2) The quadrupole structure of
 600 correlation and anti-correlation between $\overline{PMC\ OF'}$ and $\overline{T'}$ is significantly enhanced for the
 601 major-SSW season, presenting a higher absolute value of the correlation coefficient when major
 602 SSWs occur ($|r|$ +21%). This suggests that the day-to-day PMC variability in summer SH is
 603 significantly more correlated to variabilities in $\overline{U'}$ and $\overline{T'}$ during SSW events. (3) The positive
 604 correlation between $\overline{PMC\ OF'}$ and $\overline{T'}$, depicted by a large structure slanted poleward from
 605 equatorial stratosphere to high-latitude summer mesosphere for SH 2012/2013, could explain the
 606 decrease seen in PMC OF for the same season, occurring later at DSS +20. Although the
 607 permanent effect of IHC is a cooling of the high-latitude summer mesosphere, shown by
 608 Karlsson & Becker (2016) to be determined by the strength of the westward GW drag in the
 609 winter mesosphere, the increased GW activity in winter stratosphere can leads to a warmer
 610 summer polar mesosphere via a weaker residual circulation (Karlsson & Becker, 2016).

611 In conclusion, we showed that the major SSW in winter NH 2012/2013 increases the
 612 GWMF in summer SH, enhances the correlation between PMCs and GWs which are assumed to
 613 be from monsoon regions, and changes the dynamics of the global atmosphere. We also showed,
 614 by using the adjusted-lag PMC OF, that major SSWs can play a role in the destruction of PMC
 615 layers, days later in the PMC season. While the intra-hemispheric connection between low- to
 616 high- altitude summer hemisphere has been shown to influence the start of PMC season due to
 617 the persistency of the polar vortex (Gumbel and Karlsson, 2011), this study showed enhancement
 618 in IHC between winter stratosphere in NH and summer stratosphere in SH during SSWs, that in
 619 turn reduces the seasonal PMC activity. We expect to verify these observations regarding the
 620 effects of SSWs on GW propagation from troposphere in both hemispheres, in the future, using
 621 ray-tracing simulations.

622

623 **Acknowledgments and Data**

624 The TIMED/SABER data (version 2.0 level 2A) are available from the SABER website
 625 (<http://saber.gats-inc.com/data.php>). The precipitation data from TRMM/DPR are available from
 626 NASA's Data and Information Services Center website
 627 (https://disc.gsfc.nasa.gov/datasets/TRMM_3B42_Daily_7/summary). The radiation data from
 628 NOAA/AVHRR are available from NOAA's Physical Sciences Laboratory website
 629 (https://psl.noaa.gov/data/gridded/data.uninterp_OLR.html#plot). MERRA-2 simulations

630 (version 5.12.4) are available from NASA's Data and Information Services Center website
631 (https://disc.gsfc.nasa.gov/datasets/M2I6NVANA_5.12.4/summary). The PMC data from
632 AIM/CIPS are available from the Laboratory for Atmospheric and Space Physics website
633 (<http://lasp.colorado.edu/aim/download-data-L3C.php>) and PMC data from AIM/SOFIE are
634 available from the SOFIE website (<http://sofie.gats-inc.com/sofie/index.php>). This research was
635 supported by NASA Grant 80NSSC18K0650 and by NSF award 1855476.

636

637 **References**

- 638 Alexander, M. J., & Rosenlof, K. H. (1996). Nonstationary gravity wave forcing of the
639 stratospheric zonal mean wind. *Journal of Geophysical Research: Atmospheres*, 101(D18),
640 23465-23474.
- 641 Becker, E. (2004). Direct heating rates associated with gravity wave saturation. *Journal of*
642 *atmospheric and solar-terrestrial physics*, 66(6-9), 683-696.
- 643 Becker, E. (2012). Dynamical control of the middle atmosphere. *Space science reviews*, 168(1-
644 4), 283-314.
- 645 Becker, E., & Fritts, D. C. (2006). Enhanced gravity-wave activity and interhemispheric
646 coupling during the MaCWAVE/MIDAS northern summer program 2002.
- 647 Benze, S., Randall, C. E., Karlsson, B., Harvey, V. L., DeLand, M. T., Thomas, G. E., & Shettle,
648 E. P. (2012). On the onset of polar mesospheric cloud seasons as observed by SBUV. *Journal of*
649 *Geophysical Research: Atmospheres*, 117(D7).
- 650 Chandran, A., Rusch, D. W., Thomas, G. E., Palo, S. E., Baumgarten, G., Jensen, E. J., &
651 Merkel, A. W. (2012). Atmospheric gravity wave effects on polar mesospheric clouds: A
652 comparison of numerical simulations from CARMA 2D with AIM observations. *Journal of*
653 *Geophysical Research: Atmospheres*, 117(D20).
- 654 Charlton, A. J., & Polvani, L. M. (2007). A new look at stratospheric sudden warmings. Part I:
655 Climatology and modeling benchmarks. *Journal of Climate*, 20(3), 449-469.
- 656 Chu, X., Yamashita, C., Espy, P. J., Nott, G. J., Jensen, E. J., Liu, H. L., & Thayer, J. P. (2009).
657 Responses of polar mesospheric cloud brightness to stratospheric gravity waves at the South Pole
658 and Rothera, Antarctica. *Journal of atmospheric and solar-terrestrial physics*, 71(3-4), 434-445.
- 659 Cullens, C. Y., England, S. L., & Immel, T. J. (2015). Global responses of gravity waves to
660 planetary waves during stratospheric sudden warming observed by SABER. *Journal of*
661 *Geophysical Research: Atmospheres*, 12-18.
- 662 Ern, M., Preusse, P., Gille, J., Hepplewhite, C., Mlynczak, M., Russell, J., & Riese, M. (2011).
663 Implications for atmospheric dynamics derived from global observations of gravity wave
664 momentum flux in stratosphere and mesosphere. *Journal of Geophysical Research:*
665 *Atmospheres*.
- 666 Gao, H., Li, L., Bu, L., Zhang, Q., Tang, Y., & Wang, Z. (2018). Effect of Small-Scale Gravity
667 Waves on Polar Mesospheric Clouds Observed From CIPS/AIM. *Journal of Geophysical*
668 *Research: Space Physics*, 123(5), 4026-4045.

- 669 Gerrard, A. J., Kane, T. J., Eckermann, S. D., & Thayer, J. P. (2004). Gravity waves and
670 mesospheric clouds in the summer middle atmosphere: A comparison of lidar measurements and
671 ray modeling of gravity waves over Sondrestrom, Greenland. *Journal of Geophysical Research:*
672 *Atmospheres*, 109(D10).
- 673 Gumbel, J., & Karlsson, B. (2011). Intra-and inter-hemispheric coupling effects on the polar
674 summer mesosphere. *Geophysical research letters*, 38(14).
- 675 Hervig, M. E., Gordley, L. L., Stevens, M. H., Russell III, J. M., Bailey, S. M., & Baumgarten,
676 G. (2009). Interpretation of SOFIE PMC measurements: Cloud identification and derivation of
677 mass density, particle shape, and particle size. *Journal of Atmospheric and Solar-Terrestrial*
678 *Physics*, 316-330.
- 679 Jensen, E. J., & Thomas, G. E. (1994). Numerical simulations of the effects of gravity waves on
680 noctilucent clouds. *Journal of Geophysical Research: Atmospheres*, 99(D2), 3421-3430.
- 681 Kalisch, S., Preusse, P., Ern, M., Eckermann, S. D., & Riese, M. (2014). Differences in gravity
682 wave drag between realistic oblique and assumed vertical propagation. *Journal of Geophysical*
683 *Research: Atmospheres*, 10-081.
- 684 Karlsson, B., & Becker, E. (2016). How does interhemispheric coupling contribute to cool down
685 the summer polar mesosphere? *Journal of Climate*, 29(24), 8807-8821.
- 686 Karlsson, B., & Shepherd, T. G. (2018). The improbable clouds at the edge of the atmosphere.
687 *Physics today*, 30-36.
- 688 Karlsson, B., Körnich, H., & Gumbel, J. (2007). Evidence for interhemispheric stratosphere-
689 mesosphere coupling derived from noctilucent cloud properties. *Geophysical Research Letters*,
690 34(16).
- 691 Karlsson, B., Randall, C. E., Benze, S., Mills, M., Harvey, V. L., Bailey, S. M., & Russell III, J.
692 M. (2009). Intra-seasonal variability of polar mesospheric clouds due to inter-hemispheric
693 coupling. *Geophysical research letters*, 36(20).
- 694 Körnich, H., & Becker, E. (2010). A simple model for the interhemispheric coupling of the
695 middle atmosphere circulation. *Advances in Space Research*, 661-668.
- 696 Liu, H. L., & Rodle, R. G. (2002). A study of a self-generated stratospheric sudden warming and
697 its mesospheric-lower thermospheric impacts using the coupled TIME-GCM/CCM3. *Journal of*
698 *Geophysical Research: Atmospheres*, 107(D23), 4695.
- 699 Matsuno, T. (1971). A dynamical model of the stratospheric sudden warming. *Journal of the*
700 *Atmospheric Sciences* 28(8), 1479-1494.
- 701 McClintock, W. E. (2008). The cloud imaging and particle size experiment on the Aeronomy of
702 Ice in the mesosphere mission: Instrument concept, design, calibration, and on-orbit
703 performance. *Journal of atmospheric and solar-terrestrial physics*, 71(3-4), 340-355.
- 704 Preusse, P., Schroeder, S., Hoffmann, L., Ern, M., Friedl-Vallon, F., Ungermann, J., . . . Riese,
705 M. (2009). New perspectives on gravity wave remote sensing by spaceborne infrared limb
706 imaging. *Atmospheric Measurement Techniques*, 299-311.

- 707 Rapp, M., Lübken, F. J., Müllemann, A., Thomas, G. E., & Jensen, E. J. (2002). Small-scale
708 temperature variations in the vicinity of NLC: Experimental and model results. *Journal of*
709 *Geophysical Research: Atmospheres*, 107(D19), AAC-11.
- 710 Russell, J. M., Mlynczak, M. G., Gordley, L. L., Tansock, J. J., & Esplin, R. W. (1999).
711 Overview of the SABER experiment and preliminary calibration results. *Optical Spectroscopic*
712 *Techniques and Instrumentation for Atmospheric and Space Research III* (pp. 277-289).
713 International Society for Optics and Photonics.
- 714 Sato, K., Watanabe, S., Kawatani, Y., Tomikawa, Y., Miyazaki, K., & Takahashi, M. (2009). On
715 the origins of mesospheric gravity waves. *Geophysical research letters*.
- 716 Siskind, D. E., Eckermann, S. D., McCormack, J. P., Coy, L., Hoppel, K. W., & Baker, N. L.
717 (2010). Case studies of the mesospheric response to recent minor, major, and extended
718 stratospheric warmings. *Journal of Geophysical Research: Atmospheres*, 115(D3).
- 719 Siskind, D. E., Stevens, M. H., Hervig, M., Sassi, F., Hoppel, K., Englert, C. R., & Kochenash,
720 A. J. (2011). Consequences of recent southern hemisphere winter variability on polar
721 mesospheric clouds. *Journal of atmospheric and solar-terrestrial physics*, 73(13) 2013-2021.
- 722 Thurairajah, B., Cullens, C. Y., Siskind, D. E., Hervig, M. E., & Bailey, S. M. (2020). The Role
723 of Vertically and Obliquely Propagating Gravity Waves in Influencing the Polar Summer
724 Mesosphere. *Journal of Geophysical Research: Atmospheres*, 125(9).
- 725 Thurairajah, B., Siskind, D. E., Bailey, S. M., Carstens, J. N., Russell III, J. M., & Mlynczak, M.
726 G. (2017). Oblique propagation of monsoon gravity waves during the northern hemisphere 2007
727 summer. *Journal of Geophysical Research: Atmospheres*, 5063-5075.
- 728 Wright, C. J., & Gille, J. C. (2011). HIRDLS observations of gravity wave momentum fluxes
729 over the monsoon regions. *Journal of Geophysical Research: Atmospheres*.
- 730 Yamashita, C., England, S. L., Immel, T. J., & Chang, L. C. (2013). Gravity wave variations
731 during elevated stratopause events using SABER observations. *Journal of Geophysical*
732 *Research: Atmospheres*, 5287-5303.
- 733 Yasui, R., Sato, K., & Tsutsumi, M. (2016). Seasonal and interannual variation of mesospheric
734 gravity waves based on MF radar observations over 15 years at Syowa Station in the Antarctic.
735 *SOLA*, 12, 46-50.